Renewable Energy 182 (2022) 602–614

Contents lists available at ScienceDirect

Renewable Energy

journal homepage: www.elsevier.com/locate/renene

Experimental and numerical study on the preheating process of a lab-scale solar molten salt receiver

Yawei Li, Hao Zhou*, Yuhang Zuo, Mingrui Zhang

State Key Laboratory of Clean Energy Utilization, Institute for Thermal Power Engineering, Zhejiang University, Hangzhou, 310027, China

ARTICLE INFO

Article history:
Received 17 May 2021
Received in revised form
3 October 2021
Accepted 17 October 2021
Available online 21 October 2021

Keywords:
Lab-scale solar receiver
Preheating process
Thermal performance
Xenon lamps

ABSTRACT

The preheating process of the solar receiver in the Concentrated Solar Power (CSP) plant is necessary but dangerous before filling the molten salt, because the empty pipe is easy to overheat, but it is required to heat up quickly to match the preheating requirement. In this paper, a lab-scale receiver was used to study the preheating process, and a transient numerical model was also developed for a better understanding of the preheating process. A detailed description of the receiver's performance on the 20% xenon lamp power was conducted, and the numerical modeling was verified through the comparison with the experimental results. The preheating process of the receiver under different xenon lamp power was performed, and a non-linear relationship existed between the period of the preheating process and the different xenon lamp power. Moreover, this paper also reported that the negative feedback control was used to realize the dynamical preheating process, and the method worked according to the surface temperature of the receiver until the preheating requirement was reached. Finally, the effect of environmental temperature on the preheating process was conducted, and the preheating duration of the receiver with the same heat flux was prolonged by about 30 s with the environment temperature of −2 °C.

1. Introduction

Concentrated Solar Power plants generally include heliostat field, receiver, hot and cold salt tanks, and power generation equipment, such as the Solar Two, the Gemasolar, the DAHAN plants [1–3]. Thousands of heliostats are used to converge sunlight onto the receiver coated with the high-absorption coating. The light is converted into heat energy in the receiver, and then the heat energy is converted into electrical energy through a series of devices. The CSP plants have an essential contribution to reducing CO_2 emissions and help eliminate the problem of global warming.

The receiver is one of the essential equipment in the CSP plants. It works in an extremely harsh environment and generally has large thermal stress caused by the large temperature gradient. Therefore, the status of the receiver is related to the safe operation and economic benefits of the entire plant. The current research on the receiver is mainly studying its thermal performance, generally including the temperature and thermal stress in the steady or quasi-steady state, primarily using numerical modeling simulation or experimental research in the laboratory. Wang et al. [4] evaluated the optical and thermal performance of a fin-like receiver. They developed and validated a 3D model coupling the Monte Carlo Ray-tracing method and the Finite Volume method using the ANSYS Fluent software. It was found that the fin-like receiver could enhance the receiver's efficiency by 3.7% with the same receiver diameter. Zou et al. [5,6] used the ANSYS Fluent software and ESS software to investigate the thermal performance of the cavity receiver with the spiral coil and discovered that the 5 laps disk was the most effective. Rodríguez-Sánchez et al. [7] used ANSYS Fluent software and a simplified model to evaluate the performance of a tower receiver, respectively, and presented the evolution of the wall and the salt temperature. They found that using the simplified model had similar results with using CFD software. Zhou et al. [8,9] also used commercial CFD software and an in-house code to study a lab-scale molten salt receiver, respectively, and both results had good agreement with the experimental data. Zhou et al. [10] also applied the in-house code to a 600 MWth receiver and explored the thermal stress and thermal performance, and a good result was also obtained.

However, the preheating process of the receiver was needed

* Corresponding author.
E-mail address: zhouhao@zju.edu.cn (H. Zhou).

https://doi.org/10.1016/j.renene.2021.10.051
0960-1481/

before filling the molten salt, and it will otherwise cause the solidification and blockage of the molten salt during the salt filling process. The preheating processes can prove hazardous due to the need to rapidly heat up an empty tube up to the required temperature, with the potential risk of overheating that this presents. The preheating process is a transient heat transfer process, which involves unsteady heat conduction and radiation, and there is less research on this aspect at present. Fernández-Torrijos et al. [11,12] conducted a study using a single tube heated by a magnetic induction heater, using experimental and numerical simulation methods in the laboratory, and introduced preheating process under different working cases. They found a good agreement between the experimental and calculated tube temperatures and deflection, with differences of 7% and 10%, respectively. Wan et al. [13] researched the fatigue failure of two different boiling panels under the daily cold startup operation using the computation model. It was found that the non-uniform stress-strain leads to the warping of the boiling panel. The largest displacement is in the direction normal to the heat-absorbing surface toward the cavity internal, the largest displacement range is 17 cm. Lopez [14] presented a simplified model based on the theoretical model to predict the thermal startup transient of the receiver of NASA's experimental 2-kW solar dynamic (SD) system and discussed comparisons between the computational predictions and the experimental results obtained from the tests performed, and a good agreement was obtained. Hefni [15] developed a detailed dynamic model of the Solar Two receiver to evaluate the risk of salt crystallization in the receiver tubes for the gravity drainage scenario in the absence of solar irradiation and when the molten salt temperature in the pipes was calculated during the drainage of the receiver. Yang et al. [16] performed a series of tests to investigate the effects of input heating flux, and inclination angle on high temperature two-phase flat heat pipe receiver (FHPR) thermal behavior, and the result indicated that FHPR had good startup performance and isothermal properties. Yang et al. [17] also developed a transient analysis code for the novel flat heat pipe receiver (FHPR) to simulate the transient startup from the frozen state, and the analytical solutions were in good agreement with the experimental data. Wang et al. [18] investigated and analyzed the startup characteristics, isothermal performance, and thermal resistance variation of the high-temperature special-shaped heat pipe (HTSSHP) experimentally. They found that the overall thermal resistance in HTSSHP reduces with increasing operating temperature, ranging from 0.12 °C/W to 0.19 °C/W. Wang et al. [19] reported the transient performance of a prototype impinging receiver using xenon lamps, and the temperature changing rate of the receiver was within 3 °C/s for the startup process and 4 °C/s for the shut-down process. Besides, Xu et al. [20] introduced molten salt tube cold filling instead of filling molten salt into the tube after preheating process, and it can accelerate the startup of a molten salt CSP plant. Alexopoulos et al. [21] developed a mathematical model for the simulation of the unsteady-state behavior of a solar-heated rotary kiln receiver to figure out the specifics of one start-up period per day, which also contributes to the study of the preheating process of the molten salt receiver.

The preheating process of the on-site receiver is an important and complicated process, which generally takes 15–30 min [22]. The preheating process is dynamic, and the receiver was preheated generally with a uniform or non-uniform heat flux distribution. For preheating under non-uniform heat flux distribution, the areas with large flux have a higher heating rate during the preheating process. When these areas reach the maximum allowable temperature (i.e., 350 °C), the areas with small flux have not yet reached the minimum allowable temperature (i.e., 230 °C). The heliostats aimed at the high flux area were required to remove and wait for the area with small flux, but as the temperature of these areas rose, the temperature of the previously high flux area began to drop. When the temperature drops to the set value, the previously removed heliostat starts to work again. The process above was repeated until the temperature of all areas matches the preheating requirement. For preheating under uniform heat flux distribution, the temperature of the receiver all rise at the same rate, and it can avoid the complex process under non-uniform flux, but the flux of the receiver was hardly adjusted uniformly. In the Solar Two, some heliostats were selected in the preheating process of the receiver, and the flux was modified evenly through adjusting the aiming point of the heliostats, and the flux was about 20 kW/m^2 without wind and 35 kW/m^2 with wind, respectively [22]. However, the report did not have a detailed description of the preheating process, only a basic introduction.

From the above literature, the most relevant work is on the single tube heated by the electromagnetic heater [11,12], which is much different from the on-site preheating, and the Solar Two report on the preheating of the receiver is not detailed enough [22]. Therefore, the innovation of this paper is to use a lab-scale receiver under non-uniform heat flux to study the preheating process and conduct a detailed description of the receiver's performance on the preheating process combining experiments and simulations. In this paper, the lab-scale receiver coated with the high-absorption coats was warmed by 15 xenon lamps, which is more complicated than the single tube test but closer to the on-site receiver. The preheating experiments with different xenon lamps power and dynamic preheating experiments with negative feedback control were carried out on the lab-scale receiver. At the same time, the preheating process of the tube was numerically and transiently modeled, and good consistency was obtained between the experimental data and numerical prediction. Finally, the preheating process of the receiver under a low environment temperature was also studied. This work was very rare and had a guiding effect on the preheating process of the on-site receiver.

2. Experimental setup and procedures

2.1. The lab-scale receiver

The preheating process of the receiver is a dynamic process, and it was required that all parts of the receiver need to exceed 230 °C before the salt was filled because the working medium in the receiver is the solar salt, which is consist of 40% $NaNO_3$ and 60% KNO_3 by weight. The working temperature of the solar salt is in the range of 230 °C–565 °C, to prevent it from freezing at low temperature or decomposing when overheating, so the temperature distribution of the receiver would directly affect the safe and stable operation of the plant. In general, conducting experiments on the on-site plant is troublesome and costly. In order to study the startup process of the CSP plant, a lab-scale CSP plant was designed and built, including the key components such as cold and hot salt tanks, Steam Generator System, and receiver, except for power generation equipment. The specific introduction about the lab-scale plant was described in Ref [8,9]. The lab-scale receiver used solar salt as the working medium, and the tubes were coated with a high-absorption rate coating and were illuminated by 15 xenon lamps.

The lab-scale contains 6 panels, and each panel contains 3 tubes, a total of 18 tubes. The tube was made of Inconel 625 with a diameter of $\Phi 21 \times 1.2$, as shown in Table 1. The Inconel 625 had good thermophysical properties, can withstand higher temperatures, and better allowable stress. The properties of Inconel 625 were listed in Table 2, which would be used for the numerical simulation. The temperature variation of the thermal conductivity and heat capacity of the tube material was not considered in this

Table 1
Receiver's parameters.

Parameter	Value
Heat tube diameter, mm	Φ21 × 1.2
Heat absorption length, m	2.40
Single xenon lamp power, kW	2–10 (adjustable)
Number of xenon lamp	15

Table 2
Inconel 625 properties.

Property	Value
Poisson's ratio	0.308
coefficient of linear thermal expansion (10^{-6} mm^{-1} K^{-1})	12.3
Young's modulus (GPa)	205
specific heat at constant pressure (J·kg^{-1} K^{-1})	430
Thermal conductivity (W/(m·K))	12.4 (200 °C)
Density (g/cm^3)	8.44

paper, for the properties of the Inconel 625 change relatively little with temperature. The emission spectrum of xenon lamps is similar to that of the sun, using xenon lamps has seen broad acceptance as an appropriate light source to study receivers in the laboratory [5,8,9]. Each xenon lamp used in the lab-scale plant was mainly controlled by two-axis control, which can be rotated to adjust the spot position on the receiver, and the xenon lamp is pointed to the required position on the receiver when the experiment was conducted. The electric power of each xenon lamp can be adjusted from 2 kW to 10 kW.

2.2. Experimental setup

The receiver mainly converts the sunlight projected by the mirror field into heat energy. Similarly, the lab-scale receiver converts the light from the xenon lamp into heat energy. In general, the heat flux directly affects the safe operation of the receiver, so the projected heat flux is mainly measured in the experiment in advance.

When the Solar Two was preheating, it controlled the heliostats to make sure that the heat flux on the surface of the receiver was as evenly distributed as possible [22]. Therefore, the radiation map of the xenon lamps was adjusted to be as uniform as possible. Yet, a good uniformity cannot be reached because the number of xenon lamps used is too small and the spot of the xenon lamp was not small enough. The number of xenon lamps and the corresponding focusing strategy was shown in Fig. 2. The xenon lamp groups were indexed firstly, and it contained 15 xenon lamps with three rows and five columns, and the numbering of xenon lamps was shown in Fig. 2a. Then the front surface of the receiver was divided into 6 × 6 grids, and the main position on the receiver of each xenon lamp spot was marked, and as shown in Fig. 2b. Fig. 2b mainly showed the main position of the light spot of each lamp on the receiver, and the central area had a larger heat flux comparing the rest region.

After the concentrating process of xenon lamps was completed, a method combining Lambert plate and radiometer was adopted in order to measure the surface heat flux of the receiver. Ref [8] gave a detailed introduction to this method and equipment.

The surface heat flux measured of the lab-scale receiver was shown in Fig. 3, and the maximum flux was 36 kW/m^2. Besides, it could be found that the center was relatively uniform.

For temperature measurement, the frontal temperature can only be measured by the non-contact measurement method, and infrared cameras are commonly used in receiver temperature measurement [8,9,22]. In this experiment, the Testo 885–2 infrared camera produced by Testo SE & Co., was used to measure the front temperature of the receiver. The infrared camera has a wide working range of −10 °C–1000 °C and the measurement error of ±2 °C.

The temperature measurement on the back of the receiver mainly was adopted K-type thermocouples with an error of ±1.5 °C. For ease of installation, only one thermocouple was installed at the M2 position in Fig. 1a, and it was collected by the Agilent. The value of the thermocouple is mainly used for simulation verification.

It should be noted that, for the sake of simplicity, the position of the xenon lamps remained unchanged throughout the experiment, but the electrical power to the lamps was allowed to vary.

2.3. Experimental procedure

Before the Solar Two preheating process, it was necessary to turn on the electric heat tracing to preheat the pipe. Taking this into consideration, the electrical heating of the pipeline (mainly below

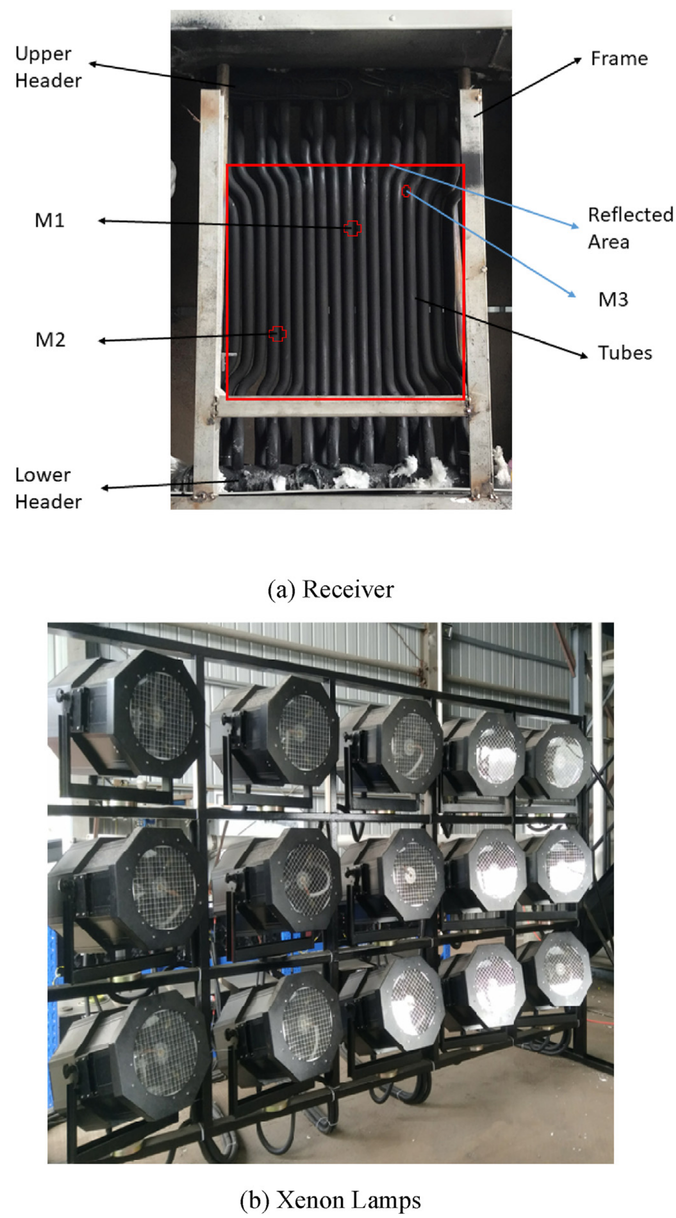

Fig. 1. Photos of the experimental setups.

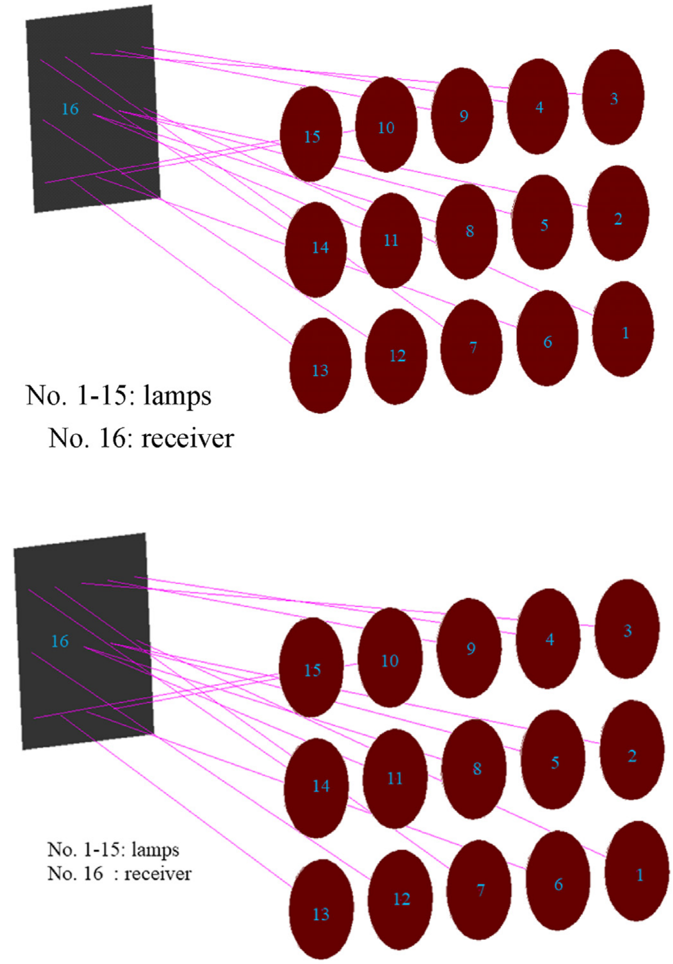

(a)

12	7,12	7,13	1,13,6	5,1, 6	5, 6
14	14,15	11,15	11	4	4
14	14,15	8,11,15	8,11	4,2	4
14,10	10	10,9,8	2,8,9	2	2
10	10	9,8,10	3,9	2,3	3
10,7	7	7	3	3	3

(b)

Fig. 2. The introduction of the aiming method of the xenon lamps (a. Indexing of lamps; b. Gridding of the receiver plane).

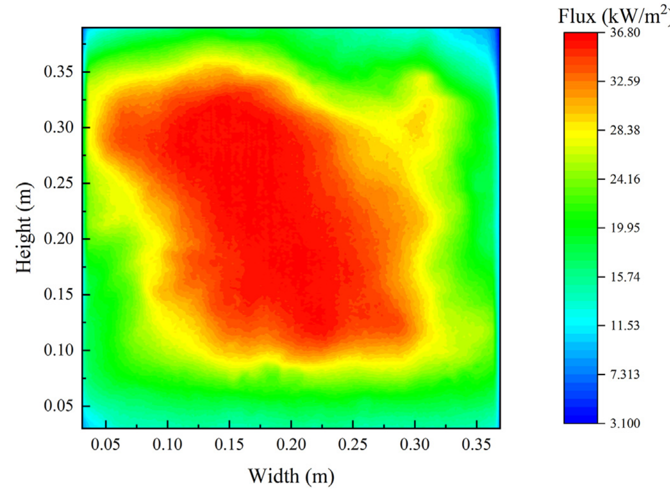

Fig. 3. The heat flux map of the receiver under 20% lamp power.

the receiver) was started before the start of the experiment. Therefore, at the beginning of the experiment, the temperature of the entire receiver was uneven, and the temperature near the header was higher.

After the preheating of electric heat tracing was completed, start the xenon lamp and use Agilent and infrared cameras to measure the temperature changes on the front and back of the receiver, respectively. During the measurement, ensure that the infrared camera was fixed in the same position, mainly for the convenience of subsequent analysis.

The case with 20% lamp power was the base case and conducted first. This work mainly explored the preheating of the receiver with fixed heat flux, dynamic heat flux, and low environment temperature preheating (−2 °C). The experimental cases were listed in Table 3.

During the preheating process, in order to prevent the receiver tube from rupturing, the heat flux was generally 20 kW, and the maximum heat flux used was constrained by the necessity of maintaining Solar Two at an operating temperature of 350 °C [22]. The completion criteria of the preheating process were that the receiver's temperature could all reach 230 °C, especially the rear temperature of the receiver (to prevent the solidification of molten salt). Therefore, during the experiment, monitoring the maximum temperature of the receiver was essential and necessary. The maximum allowable temperature was set at 360 °C, and the xenon lamp power needs to be reduced or turned off once it exceeded 360 °C.

3. Numerical modeling

Due to the limited experimental measurement and lack of non-generality, it is necessary to develop a numerical model for the evaluation of the receiver to save cost.

3.1. Heat transfer analysis

When the tube is absorbing heat, the tube surface of the receiver radiates energy to the surroundings. In the tube wall, the heat absorbed diffused in three dimensions. Since the inside of the tube is air, natural convection was not considered in the tubes, and only the radiation from the front wall to the rear wall was considered. Fig. 3 presented the heat flux map on the receiver, and it can be seen that the heat flux at most positions of the heat absorption tube

Table 3
Experimental cases.

Cases	Ambient temperature	Xenon lamp power	End criteria
Exp 1	13 °C	20%	reached 360 °C
Exp 2	13 °C	30%	reached 360 °C
Exp 3	13 °C	40%	reached 360 °C
Exp 4	13 °C	Dynamic	Reached even temperature distribution
Exp 5	−2 °C	20%	reached 360 °C

did not vary much especially the center position. Therefore, it was assumed that there was no heat exchange along the axial direction of the heat absorption tubes for simplicity. The temperature difference of the heat absorption tubes was mainly distributed in the cross-section. The convective heat transfer coefficient was much smaller in the tube than the radiation heat transfer and this coincidence with an assumption made by the authors [11,12]. For the sake of simplification, the heat exchange among the pipes is not considered. The results based on the above assumptions would coincide with the experimental results when the input heat flux was enough large because the axial heat conduction of the tubes and the heat exchange between the tubes could be ignored comparing the large input heat flux. However, when the heat flux of the heat absorption tube was too small, the effect of the axial heat conduction of the tubes and the heat exchange between the tubes became obvious, which would cause the calculation result and the experimental result to deviate greatly. Therefore, it was necessary to introduce a correction coefficient to offset the influence of the axial heat conduction of the heat absorption tube and the heat transfer between the tubes when the receiver was with small input heat flux.

During the preheating process, the front surface of the receiver (towards the xenon lamp) was subjected to the heat flux from the xenon lamp. The back surface is close to the insulating surface, so the temperature of the front side would be higher than the temperature of the backside, so the front wall will radiate to the back wall. At the same time, the surface will radiate energy to the environment. The thermal analysis of the tube was shown in Fig. 4a. The general governing differential equation for the transient heat conduction of the two-dimensional plane in a cylindrical coordinate system was as Eq. (1). For numerical simulation, the cross-section of the heat absorption tube was meshed and numbered. The circumferential direction is divided into 360, and the radial direction is divided into 8. In the simulation process, each grid was considered to be the same in temperature. The whole preheating process is transient heat conduction, and each unit was mainly affected by the surrounding four units, as shown in Fig. 4b. According to the conservation of energy, the temperature rise of each unit in unit time $\Delta\tau$ was caused by the energy introduced by the surrounding four units. The control equation of the whole process is shown in Eq. (2), where t represents temperature, i represents time series, and r_m is the mth layer radius.

$$\rho c_p \frac{\partial t(r,\theta,\tau)}{\partial \tau} = \frac{\lambda}{r}\left(r\frac{\partial t(r,\theta,\tau)}{\partial r}\right) + \frac{\lambda}{r^2}\frac{\partial t(r,\theta,\tau)}{\partial \theta^2} \tag{1}$$

$$\frac{\lambda\cdot(r_m-\Delta r/2)\cdot\Delta\theta}{\Delta r}\left(t^i_{m-1,n}-t^i_{m,n}\right)+\frac{\lambda\cdot(r_m+\Delta r/2)\cdot\Delta\theta}{\Delta r}\left(t^i_{m+1,n}-t^i_{m,n}\right) + \frac{\lambda\Delta r}{r_m\cdot\Delta\theta}\left(t^i_{m,n+1}+t^i_{m,n-1}-2t^i_{m,n}\right)=\frac{c_p\rho\cdot r_m\Delta r\Delta\theta}{\Delta\tau}\left(t^{i+1}_{m,n}-t^i_{m,n}\right) \tag{2}$$

Finally, the explicit difference equation of the transient conduction was obtained as Eq. (3).

$$t^{i+1}_{m,n}=\frac{a\Delta\tau}{\Delta^2 r}\left(t^i_{m+1,n}+t^i_{m-1,n}\right)+\frac{a\Delta\tau}{(r_m\Delta\theta)^2}\left(t^i_{m,n+1}+t^i_{m,n-1}\right) + \left(1-2\frac{a\Delta\tau}{\Delta^2 r}-2\frac{a\Delta\tau}{(r_m\Delta\theta)^2}\right)t^i_{m,n} \tag{3}$$

The boundary condition was essential for the temperature calculation, and different boundary conditions can lead to different temperature distributions of the whole field. As for the tubes, the outer wall received the radiation flux from the xenon lamp. Meanwhile, they lost the energy to the surrounding through heat convection and radiation. The energy conservation of the outer wall

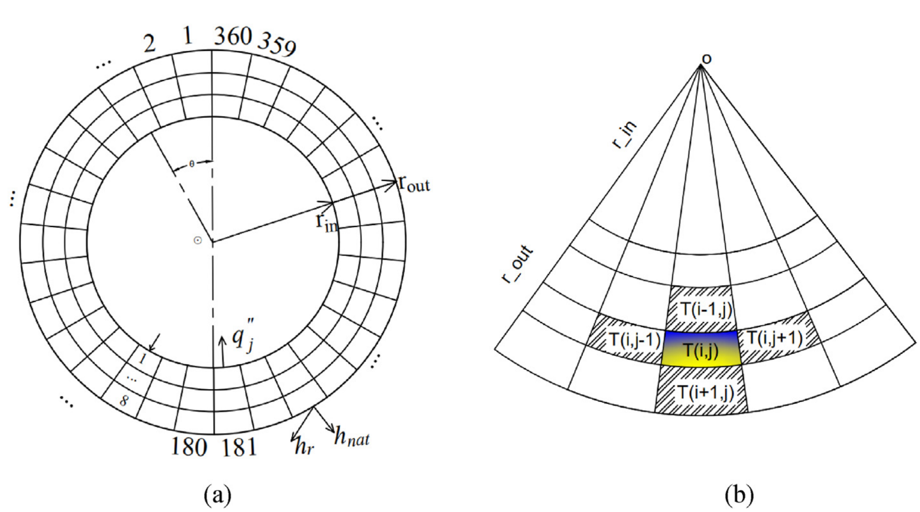

Fig. 4. The heat transfer analysis of the tube.

can be described by Eq. (4), and Eq. (5) was derived from Eq. (4). Eq. (5) was an explicit difference form that can be easily programmed, where $h_{m,n}$ represents the sum of the natural convection heat transfer coefficient and the radiation heat transfer coefficient outwards the surrounding without considering the forced convection heat transfer because no wind existed in the whole test, and $q_{M,n}$ notes the radiation heat flux of the outer wall from the xenon lamps at the ith time step. Moreover, the total heat transfer coefficient $h_{M,n}$ can be calculated using Eq. (6).

$$-\lambda\frac{\partial t(r,\theta,\tau)}{\partial r}=h_{M,n}(t(r,\theta,\tau)-T_{amb})-q_{M,n}at\ r=r_o \tag{4}$$

$$t_{M,n}^{i+1}=\frac{a\varDelta\tau}{\varDelta^2 r}t_{M-1,n}^{i}+\frac{a\varDelta\tau}{(r_M\cdot\varDelta\theta)^2}\left(t_{M,n+1}^{i}+t_{M,n-1}^{i}\right)+\frac{h_{M,n}^{i}\varDelta\tau}{\rho c_p\varDelta r}t_f+\frac{q_{M,n}^{i}\varDelta\tau}{\rho c_p\varDelta r}+\left[1-\frac{a\varDelta\tau}{\varDelta^2 r}-2\frac{a\varDelta\tau}{(r_m\cdot\varDelta\theta)^2}-\frac{h_{M,n}^{i}\varDelta\tau}{\rho c_p\varDelta r}\right]t_{M,n}^{i} \tag{5}$$

$$h_{M,n}^{i}=h_{nat}^{i}+\eta\cdot\varepsilon_c\cdot\sigma\cdot(t_{M,n}+t_{amb})\left(t_{M,n}^2+t_{amb}^2\right) \tag{6}$$

However, the inner wall of the tube had very different boundary conditions from the outer wall. The front temperature of the inner wall (towards the xenon lamp) was generally higher than the rear temperature so that the front inner wall would warm the rear inner wall through heat conduction and radiation. Therefore, the energy conservation of the inner wall can be expressed as Eq. (7), and Eq. (8) was the explicit difference form of Eq. (7), where $q_{1,n}$ represents the net radiation flux outward to the surrounding units from the unit, which can be obtained through the net flux method, as Eq. (9).

$$-\lambda\frac{\partial t(r,\theta,\tau)}{\partial r}=-q_{1,n}at\ r=r_i \tag{7}$$

$$t_{1,n}^{i+1}=\frac{a\varDelta\tau}{\varDelta^2 r}t_{2,n}^{i}+\frac{a\varDelta\tau}{(r_1\cdot\varDelta\theta)^2}\left(t_{1,n+1}^{i}+t_{1,n-1}^{i}\right)+\frac{q_{1,n}^{i}\varDelta\tau}{\rho c_p\varDelta r}+\left[1-\frac{a\varDelta\tau}{\varDelta^2 r}-2\frac{a\varDelta\tau}{(r_1\cdot\varDelta\theta)^2}\right]t_{1,n}^{i} \tag{8}$$

$$m=1,\ldots,360$$
$$\sum_{j=1}^{360}\left[\frac{\delta_{m,j}}{\varepsilon_j}-\left(\frac{1}{\varepsilon_j}-1\right)F_{m,j}\right]q_j^{''}=\sum_{j=1}^{360}\left[\delta_{m,j}-F_{m,j}\right]\sigma\cdot t_j^4 \tag{9}$$

Besides, the initial condition of the temperature field of the receiver is important for the solving the temperature field equations, and generally different initial condition maybe causing the different temperature evolution. The initial condition of the receiver preheating process was expressed as Eq. (10), where the T_{init} denoted the initial temperature of the receiver.

$$t(r,\theta,\tau)=T_{init}at\tau=0 \tag{10}$$

3.2. Numerical solution procedure

Since the explicit difference form is used in the numerical simulation process, the iteration process will diverge if the unit time was too large. If the time step is too small, the iteration process will cost a long time. Although the program stability of the explicit differential form is weak, its stability was related to the Fourier number of the lattice, which demands that unit time should be extremely small to meet the stability constraints [23]. Yang and Tao [24] believed the Lattice Fourier number cannot exceed 0.5 in order to make the program converge. The unit time in this article is 0.001 s, and the Fourier number of the lattice does not exceed 0.5, which enabled the iterative process to converge, and the calculation speed was acceptable.

The receiver was coated with Pyromark 2500, a high-absorbance black paint, whose absorbance was about 0.93 in general [8–10]. However, the lab-scale was built several years ago, and its coating was a little damaged and failed, so the absorbance of the receiver was set as 0.73, and the tubes' emissivity was set as 0.7, which can be measured roughly using the infrared camera combined with the thermocouple. The above assumption was mostly based on the heating process of the tubes, when the input radiation flux was much greater than thermal conductivity and thermal radiation convection. However, the calculation results based on the above assumptions would have large errors when the heat flow of the heat absorption tube was small or the xenon lamps were turned off. In order to solve this problem, a correction coefficient, η, was introduced in Eq. (9), which was used to express the effect of the axial heat conduction of the heat tubes. When the xenon lamp was turned off, the value of η was 0.2; when the heat tubes were rapidly heated, the value of η was set to 1.

The heat flux of the crossed-section calculation using the numerical method was prior ensured through Fig. 2. The code mainly used Eq. (3) and all boundary conditions to calculate the temperature distribution, and the code was ended according to the experimental time.

4. Results and discussion

4.1. The benchmark test and the modeling verification

As the benchmark test, the power of the Xenon lamps was 20% in the case of Exp.1, and the flux map on the receiver was shown in Fig. 3. The receiver was preheated under the fixed flux during the whole process, and the process was stopped when the maximum allowable temperature occurred. Fig. 5 displayed the temperature contours of the receiver before the test and at the end of the test. It was found that the receiver had large temperature differences before the test, as shown in Fig. 5a because the lower header of the receiver was influenced by the electrical heat-tracing system, so the temperature near the lower header was too large. Fig. 5b gave the frontal temperature contour of the receiver captured by the infrared camera when the maximum temperature of the receiver reached 360 °C, called the Maximum allowable temperature value (MAT). In Fig. 5b, the high-temperature region was in the receiver's center, and the standard deviation (SD) of the contour was 54.74 °C. Besides, the corner temperature of the receiver was too low, about 100 °C, so it didn't match the preheating criteria.

The numerical method was also used to study the preheating process of Exp.1, and the locations M1 and M2 (see Fig. 1) were selected to analyze the receiver's performance. Fig. 6 showed the temperature evolution curve of two locations during the preheating period, and the line and square represent the numerical and experimental results, respectively. It can be found that the numerical prediction had good agreement with the experimental result, especially for M1, which was warmed by 30 kW/m^2 heat flux. When the M1 temperature reached 360 °C, all Xenon lamps were closed. It can be seen that the average heating rate of M1 is 1.13 °C/s. After there is no heat flux, the receiver began to cool down. It can be seen that before the temperature was reduced to 500 s, the simulation and the experiment were in good agreement, but the simulation drops faster than the experiment beyond 500 s.

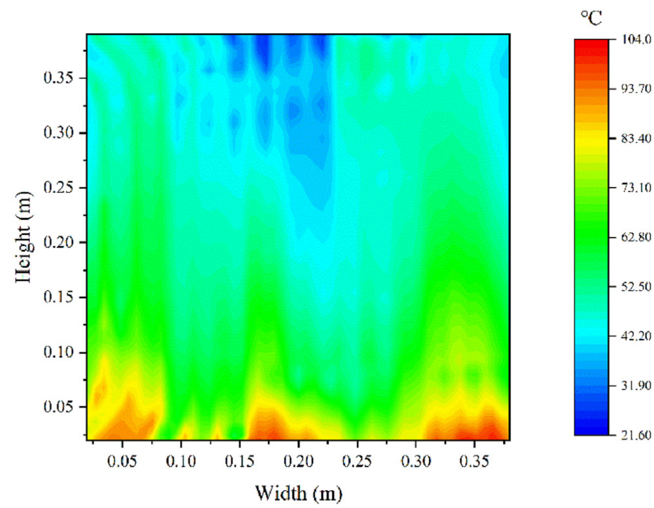

(a) preheating startup

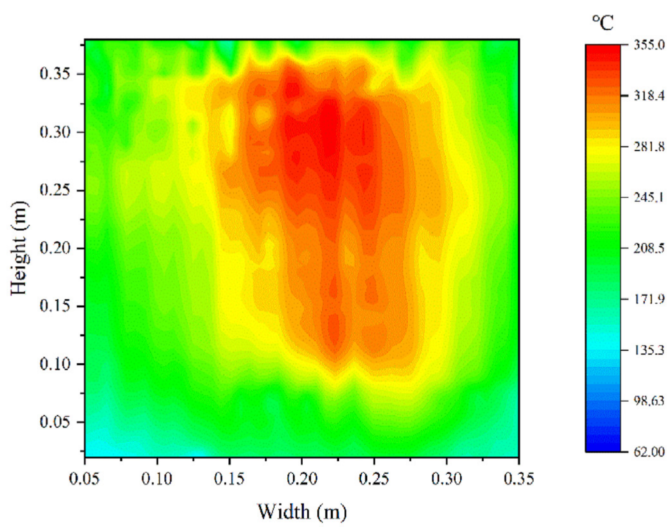

(b) preheating complication

Fig. 5. Temperature distribution before and after preheating.

This is mainly due to the existence of electric heat tracing below the lab-scale, and the electric heat tracing system will hinder the heat dissipation of the receiver to a certain extent, and the inhibitory effect was obvious when the tube wall was at low temperatures. When the temperature dropped to a certain low level, the suppression effect of the electric heating tracing system began to take effect. But the inhibitory effect of the electric heat tracing system was not considered in the simulation process, so the experiment and simulation data were not matching at all beyond 500 s. That is to say, the temperature drop was mainly affected by heat radiation between 274 s and 500 s. The heat flux received by M2 is 22 kW/m^2, and a thermocouple was installed on the back of this position. Therefore, in the results comparison of M2, an additional comparison between the frontal wall temperature and the rear wall temperature at the same time. It could be seen that the simulated temperature was higher than the experimental temperature during the heating process. The main reason is that the area was close to the corner, and some heat of the high-temperature area was

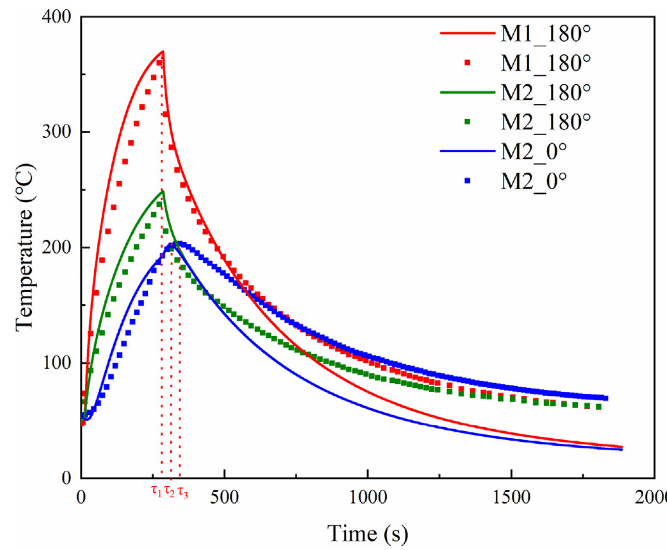

Fig. 6. The comparison between experimental and numerical results (τ_1:274s; τ_2:304s; τ_3:330s).

transferred to the low-temperature area in the corner. Besides, the back-wall temperature was lower than the front wall temperature, so after turning off the lamps for a while, the front wall still heated the back wall, so the back wall would still increase. That is to say, the temperature of the back was mainly affected by the temperature of the front via the heat radiation and thermal conductivity of the front wall. This phenomenon was manifested in both the experiment and the simulation, and the time length was 54 s for the experiment and 30 s for the simulation, respectively, which was mainly caused by the discrepancy between the boundary conditions assumption and the actual situation.

Through the comparative analysis of experiments and simulations, the simulation result was very effective, which could help obtain results that were difficult to measure in experiments. Fig. 7 respectively introduces the cross-sectional temperature distribution of M1 and M2 after the preheating starts and at the end, which can be used for stress calculation and is impossible to do in experiments. It could also be clearly seen that although the front wall temperature ($\theta = 180°$) was high at the end, the back temperature ($\theta = 0°$) was much lower, especially for M2, the back temperature was about 110 °C. Therefore, it was challenging to meet the preheating requirements using only a fixed heat flux.

4.2. Preheating process of the lab-scale receiver under different heat flux

In order to study the preheating behavior of the receiver under different heat flux, a series of experiments were conducted. The heat flux of the receiver was affected by the xenon lamp power and aiming method, and the xenon lamp direction was fixed, and the heat flux was adjusted by xenon lamp power. Exp. 1, 2 and 3 used 20%, 30% and 40% xenon lamp power respectively. For convenient analysis, the M1 point was selected to research the preheating behavior of the receiver under different heat flux.

Fig. 8 presented the temperature evolution curves of M1 under 20%, 30%, and 40% xenon lamp power, and the corresponding heat fluxes were 30 kW/m^2, 43 kW/m^2, and 55 kW/m^2. It can be seen that the preheating periods were 274 s, 106 s, and 58 s, respectively, and the corresponding average heating rates were 1.14 °C/s, 2.95 °C/s, and 5.40 °C/s. At the same time, it can be seen that the simulation and experimental results were in good agreement. Fig. 9 showed

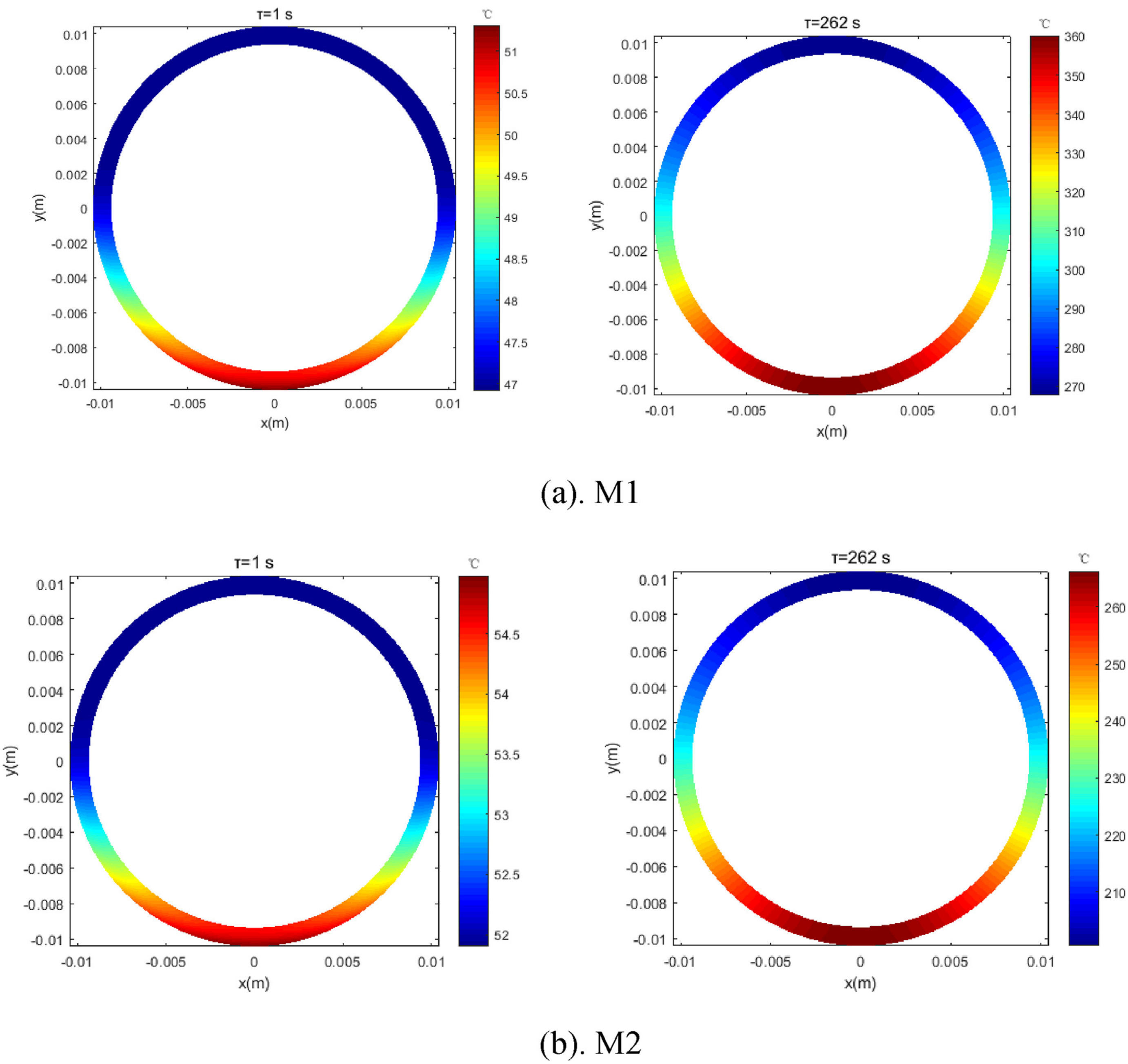

Fig. 7. The temperature maps of the crossed section on the benchmark test.

the non-linear relationship between preheating time and heat flux, in which the numerical method was used to supplement the preheating duration (blue circle point in Fig. 9) when the heat flow was 38 kW/m^2.

Fig. 10 showed the temperature distribution maps of the receiver at 30% and 40% xenon lamps power, which were similar to the temperature distribution of the benchmark test, and the standard deviation of the frontal surface temperature was about 54 °C. However, it can be found in Fig. 9 that the shorter the preheating time, the greater the temperature difference between the front and rear wall surfaces, and the greater the thermal stress at this time. Therefore, it was not appropriate to use a larger heat flux to preheat. One reason is that once it was too late to adjust, and it was easy to overheat the tube. The other reason was that the thermal stress was too large, which might easily cause pipe rupture.

4.3. Dynamic preheating process

From the above series of fixed heat flux experiments, it can be seen that the temperature distribution using the fixed heat flux is uneven, and the back temperature is also lower, which cannot meet the preheating requirements. Therefore, the preheating process under dynamic heat flow was studied, which was mainly used negative feedback control based on wall temperature combined with manual adjustment of the xenon lamps power. Due to the unevenness of heat flux, some locations would be with over-temperature (over 360 °C), so monitoring and temperature adjustment of these locations is an important part of the preheating process. In this experiment, the high-temperature position was controlled during the preheating process so that all position temperature was below 360 °C. The main theoretical basis is that use an

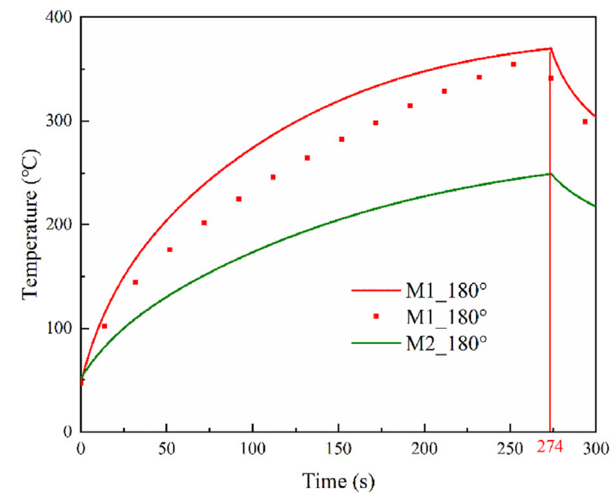

(a). 30 kw/m^2 (20% xenon lamp power)

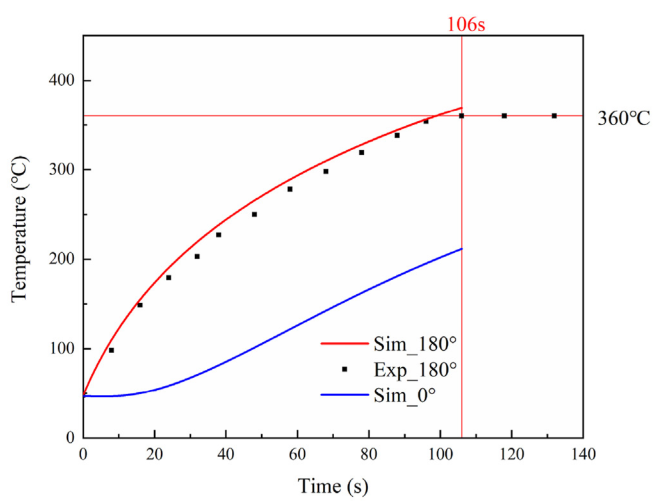

(b). 43 kW/m^2 (30% xenon lamp power)

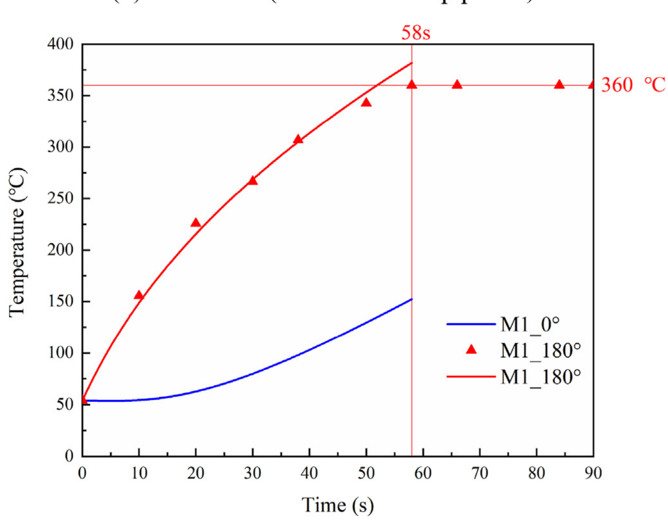

(c). 55 kW/m^2 (40% xenon lamp power)

Fig. 8. The temperature curves of M1 under different flux.

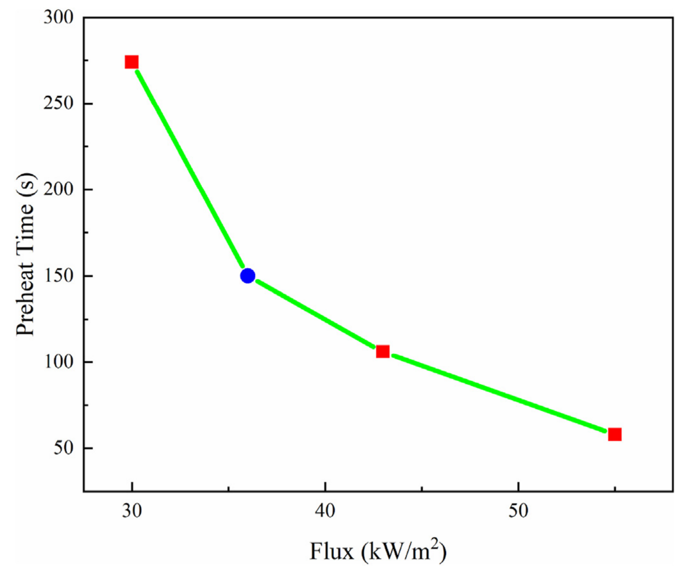

Fig. 9. The relationship between the preheating period and heat flux.

infrared camera to measure the high-temperature position of the receiver, and then start and stop the xenon lamp or adjust the load accordingly to reduce the temperature in the high-temperature zone without affecting the low-temperature area according to the xenon lamps focusing strategy. Lamps were re-projected, and the previous high-temperature region was heated when the temperature here dropped below 300 °C. The above cycle is repeated so that the temperature of each position of the receiver finally reached the preheating requirement, thereby completing the preheating. Note that during the experiment, the direction of the xenon lamp was not adjusted.

From the results of Exp.1 under the 20% xenon lamp power, it could be seen that the temperature near M1 was heated up faster, while the heat flux around the four corners was small, and the heating rate of the area near the corners was low. During the whole dynamic adjustment process of Exp.4, the heat flux was controlled according to the temperature distribution taken by the infrared camera, and the heat flux would be weakened in the over-temperature area, while the radiant heat flow would be increased in the low-temperature area. Table 4 listed the xenon lamp adjustment records during the entire dynamic preheating process of Exp.4, and Table 5 listed the changes in heat flux at positions M1, M2, and M3 over time. Compared with the 20% xenon lamp power at the start of Exp.1, the dynamic process increased the power of the No. 10 lamp to 40% at the initial stage to increase the heating rate of the lower-left corner area. Fig. 11 showed the temperature evolution curves of three typical positions, seeing Fig. 1 for details, where M3 was located on the gap between the two tubes. It could be seen from Fig. 11 that the temperature of M1, M2, and M3 rise rapidly between 0 and 230 s until the maximum temperature of M1 and M2 crossed-section reached 360 °C at $\tau = 230$ s, and the xenon lamps that mainly irradiated these areas were turned off, such as No. 8, 9, 11, 15 and 10 lamp, and the average heating rate of M1, M2, and M3 in this interval were 1.36 °C/s, 1.30 °C/s, and 0.56 °C/s, respectively. It could be found that the temperature of M1 and M2 begins to drop after these lamps were turned off, but the temperature of M2 drops the fastest because M2 was mainly affected by the No. 10 lamp, and there was still small flux on the M1 area from the rest lamps.

Similarly, the temperature of M3 was still increasing at a low rate after turning off those lamps, for the radiation received became

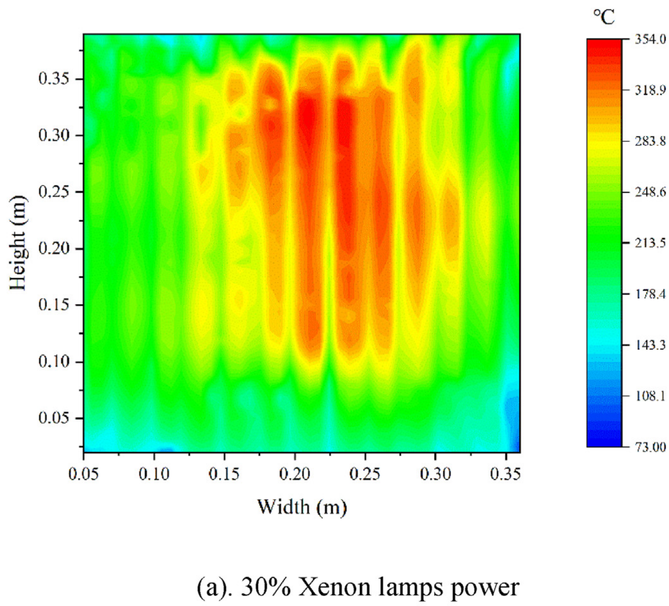

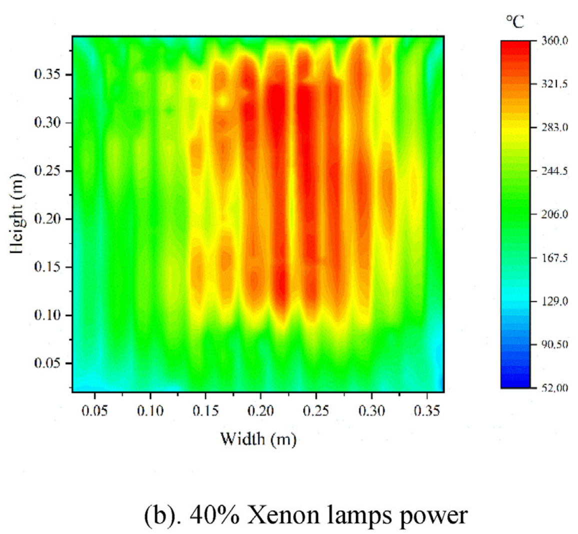

Fig. 10. The front temperature distribution of the receiver.

smaller. The temperature of M2 dropped to about 285 °C at $\tau = 294$ s, and then re-turned on the No. 10 lamp to 20% power. During this period, the rear temperature of M2 was about 230 °C. However, after a while, the temperature still dropped after a period of temperature rise, indicating that the heat flux at this location was not

Table 5
The heat flux recording on the locations M1, M2 and M3.

Stages (s)	M1 flux (kW/m^2)	M2 flux (kW/m^2)	M3 flux (kW/m^2)
0–230	32	30	15
230–294	12	5	10
294–386	12	10	10
386–536	14	18	10
536–836	14	11	10
836–926	12	11	8
926–1068	8	11	8
1068–1120	8	11	8
1120–1442	14	11	10
1442–2370	0	0	0

enough to offset the energy lost here. Then the power of the No. 10 xenon lamp increased to 30% at $\tau = 386$s, after which it can be seen that the temperature of M2 started to grow, but the temperature rise rate was less than the temperature rise rate between 0 and 230 s. It has been noticed that the frontal temperature of M1 stabilized at the range of 386 s and 826 s after the temperature dropped to about 325 °C. During this period, the heat flux at this location did not change with about 14 kW/m^2, indicating that the 14 kW/m^2 was the desired flux of this area to reached 325 °C. At the time $\tau = 536$ s, to prevent the temperature of M2 from being too high, the power of the Xenon lamp 10 was reduced to 20%, after which the M2 temperature began to drop. When it reached about 300 °C, the temperature did not change, so the desired flux of M2 to reach 300 °C was 11 kW/m^2. In addition, the desired flux for each location to reach a certain temperature could be calculated in advance by simulation, and controlling the heat flux at that location to the desired flux could achieve the desired temperature range in subsequent experiments.

Unlike M1 and M2, M3 was located in the gap between the pipes (or at the $\theta = 90°$ position of the tube), so it was necessary to do the simulation of the pipes adjacent to M3. Fig. 11c showed the temperature evolution curve of M3, and it can be seen that the simulation results were in good agreement with the experimental results. When the preheating process was ended, at $\tau = 1442$ s, the gap temperature reached approximately 220 °C.

As shown in Fig. 12, the temperature evolution curves of the heat pipe at different positions in the half-cycle were present considering account the symmetry of the pipe. It can be found that the time for the front and rear walls ($\theta = 180°$ and $0°$) to reaching the peak temperature was 230 s and 277 s, respectively, with a time difference of 47 s, similar to Fig. 6. When the whole preheating was over ($\tau = 1442$ s), the lab-scale receiver cooled freely, and it can be found that the front and rear wall temperatures started to be equal at $\tau = 1573$ s, and then the cross-sectional temperature of the heat absorber was evenly distributed after that.

After the preheating was completed, the temperature distribution on the front side of the receiver was shown in Fig. 13. It could

Table 4
The recording of the xenon lamps power adjustment.

Time (s)	State
0	Turned on all lamps, Except for the No. 10 lamp with 40% power, the rest were with 20% power.
230	Turned off No. 8, 9, 11, 15 and 10 lamps
294	Turned on the No.10 lamp with 20% power
386	Enlarged the No.10 lamp power to 40%
536	Enlarged the No.3 lamp to 30%, and turned down No.10 lamp power to 20%
836	Turned off the No.7 lamp
926	Turned off the No.13 lamp
1068	Turned down the No. 3 lamp power to 20%
1120	Turned on the No. 13 lamp with 20% power
1442	Turned off all lamps

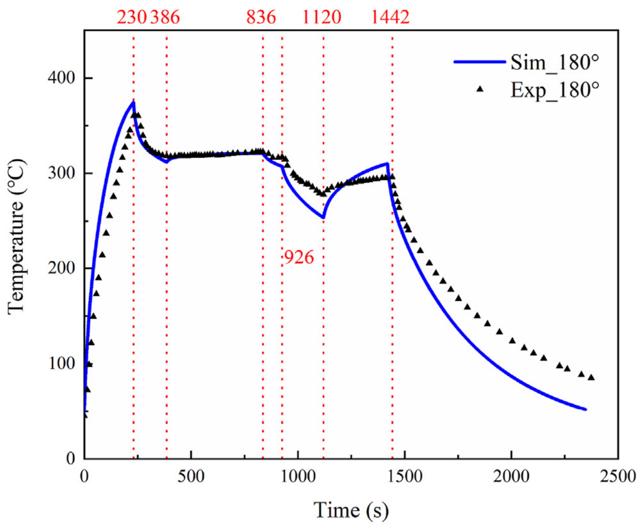

(a). M1

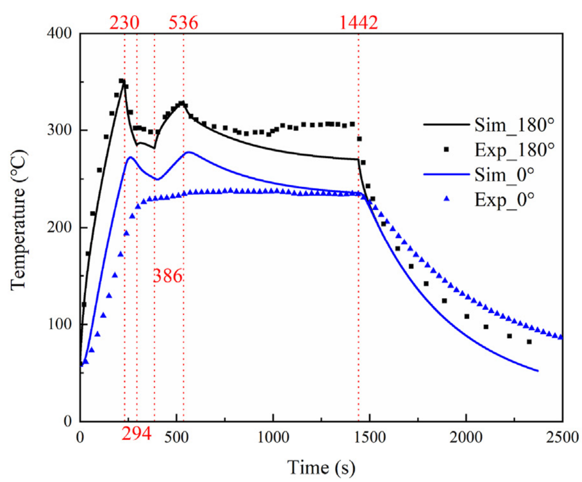

(b). M2

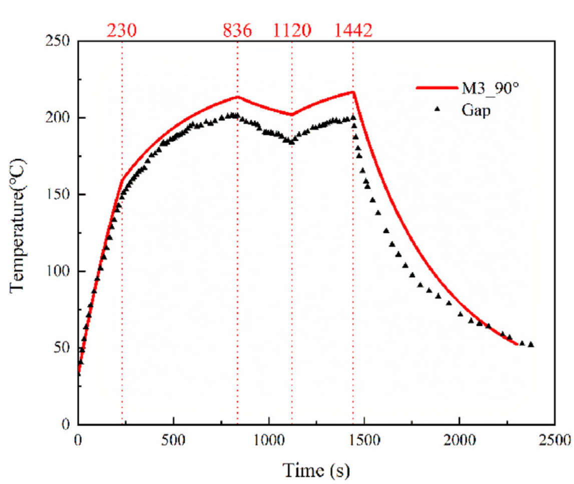

(c). M3

Fig. 11. The temperature evolution of M1, M2, and M3 during the dynamic preheating process.

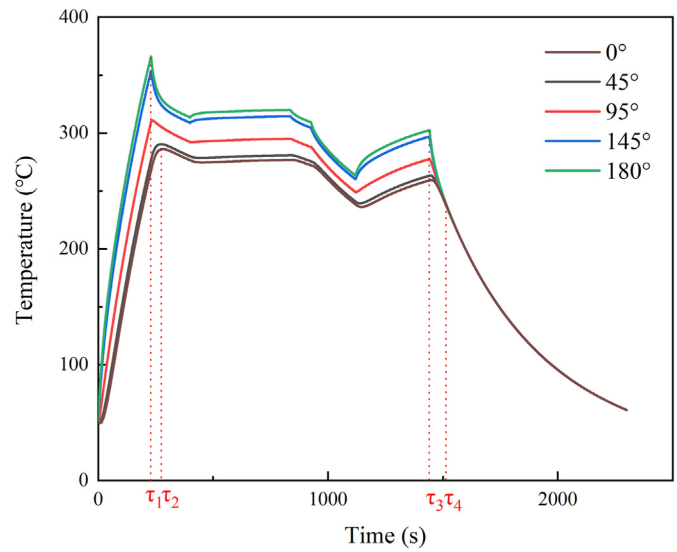

Fig. 12. The temperature evolution along the circumference at M1 crossed section (τ_1:230s, τ_2:277s, τ_3:1442s, τ_4:1573s).

be found that the temperature was more uniform compared with Fig. 5, and the standard deviation of Fig. 13 was 32 °C, dropped by 23 °C. Fig. 14 shows the cross-sectional temperature cloud diagram at M1 and M2 when the preheating is completed. It can be seen that the temperature is between 230 and 300 °C, which meets the preheating requirements.

4.4. The effect of the ambient temperature

At present, there is no relevant research on the influence of ambient temperature on the preheating of the receiver. Some CSP plants were always built near the desert, where the temperature difference between day and night was large, and some receivers sometimes started to operate under low surrounding temperature conditions, such as in Northwest China, where the environment temperature in the morning was below 0 °C in winter. Generally speaking, the preheating process of the receiver was more susceptible to environmental influences. Therefore, it is of great importance to study the effect of ambient temperature on the preheating process of the receiver.

Exps.1-4 were all carried out under the environment of 13 °C, but Exp.5 was carried out under the environment temperature of −2 °C, seeing Table 3 for details. Fig. 15 presents the comparison of the temperature at M1 under environment temperature of 13 °C and −2 °C, and the preheating periods were 230 s and 266 s when heating the tube from environment temperature to 360 °C respectively. One reason was that when the environment temperature was low, more energy output was required to warm the tube to 360 °C. The other reason was that when the ambient temperature was low, the energy loss to the surroundings through the radiation and convection was more. In addition, it could be found that the maximum rear temperature was respectively about 242 °C and 230 °C, at environment temperature of 13 °C and −2 °C, with a drop of about 12 °C, which was near the difference of the ambient temperature.

Therefore, when starting in a low-temperature environment, the receiver should take more time and absorb more energy, which will increase the operating cost of the electric field and be not conducive to the stable operation of the power plant.

5. Conclusion

The preheating process of the on-site receiver was an important and complicated dynamic process, which generally took 15–30 min. In this work, experiments and numerical modeling on the preheating process of a lab-scale receiver were performed, and it was found that the results of the experiment and simulations were in good agreement. This work provided a theoretical basis for the preheating of the on-site receiver, and some remarks were listed as following:

1. This work explored the preheating process of the lab-scale receiver under different heat flux and gave a detailed introduction to the temperature evolution and heating rate of the receiver during preheating. It was found that the preheating periods of the receiver were 274 s, 106 s, and 58 s, respectively, and the corresponding average heating rates were 1.14 °C/s, 2.95 °C/s, and 5.40 °C/s under 20%, 30%, and 40% xenon lamp power.
2. The preheating process of the lab-scale receiver under dynamic heat flux was described in detail. The receiver reached the end of preheating process at 1442 s, and the cross-sectional temperature of M1 and M2 was between 230 °C and 300 °C, and the standard deviation of front wall surface temperature was 32 °C, with a drop of 23 °C.

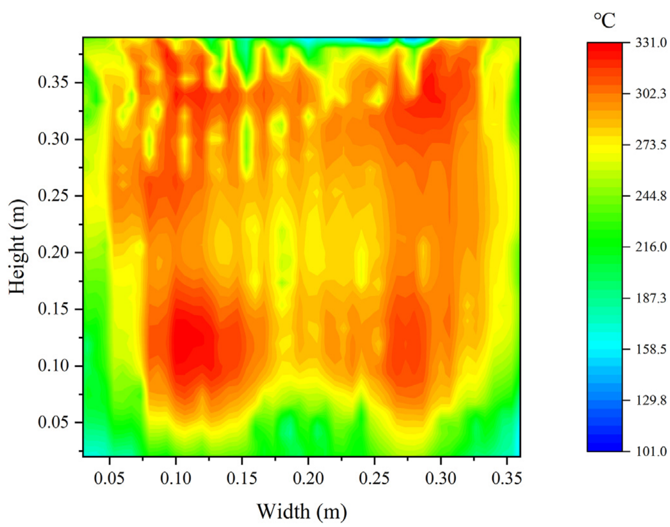

Fig. 13. the front temperature contour of the receiver when the dynamic preheating process completed.

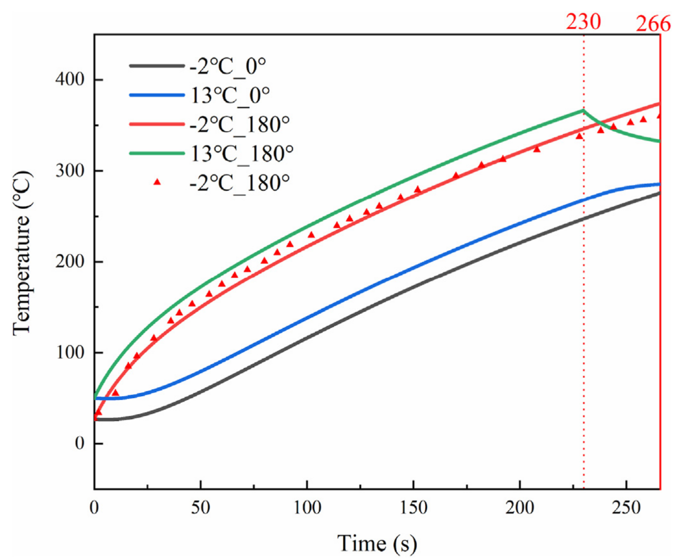

Fig. 15. Comparison of M1 temperature under the different ambient temperature.

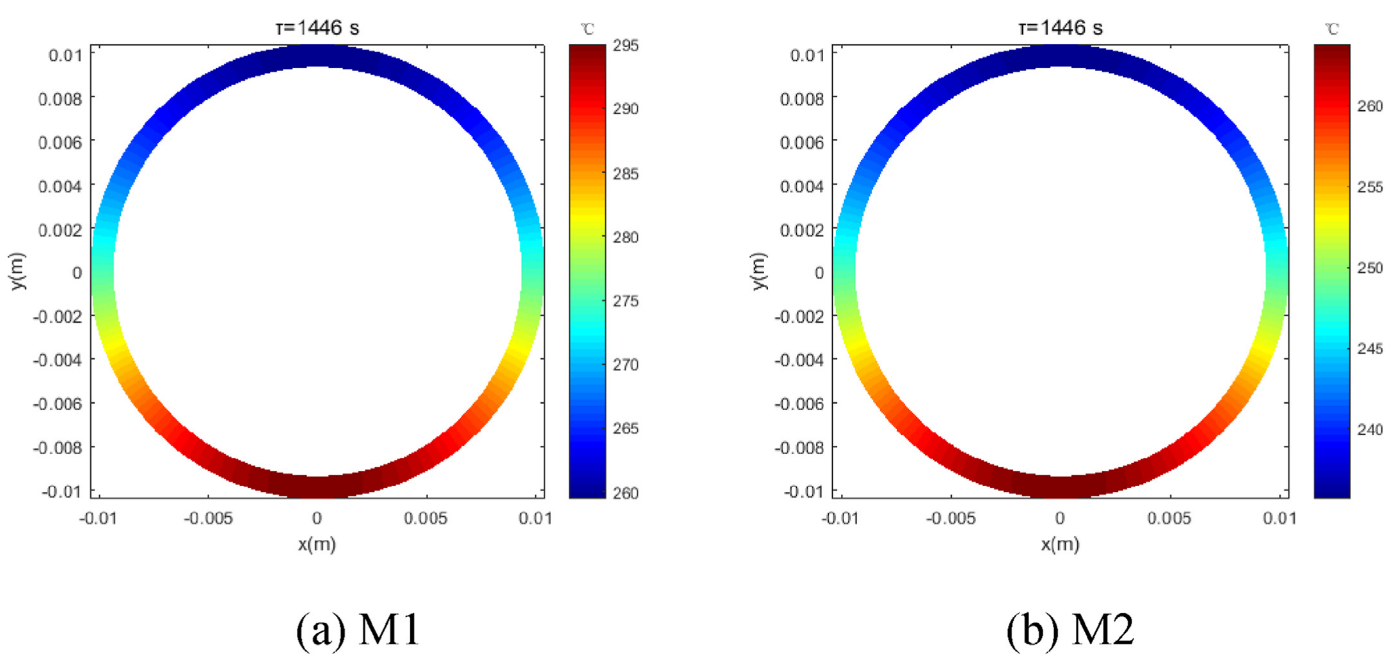

Fig. 14. The crossed-section temperature contour when the dynamic preheating process completed.

3. This paper also studied the preheating process at low ambient temperature and found that the maximum rear temperature of the receiver was respectively 242 °C and 230 °C when the ambient temperature was 13 °C and −2 °C, with a drop of 12 °C, which was the same as the difference of the ambient temperature.

Author contribution statement

Yawei Li: Methodology, Data curation, Writing-Original draft preparation. **Hao Zhou:** Conceptualization, Project administration. **Yuhang Zuo:** Software, Validation. **Mingrui Zhang:** Writing-Reviewing and Editing, Formal analysis.

Acknowledgments.

CRediT authorship contribution statement

Yawei Li: Methodology, Data curation, Writing – original draft, preparation. **Hao Zhou:** Conceptualization, Project administration. **Yuhang Zuo:** Software, Validation. **Mingrui Zhang:** Writing – review & editing, Formal analysis.

Declaration of competing interest

The authors declare that they have no known competing financial interests or personal relationships that could have appeared to influence the work reported in this paper.

This research did not receive any specific grant from funding agencies in the public, commercial, or not-for-profit sectors.

Nomenclature

t	The temperature of the grid
a	The thermal diffusivity
c_p	The specific heat capacity
F	The view factors
h	The heat transfer coefficient
q	The net flux outward to the surroundings from the grid
r	The local radius of the grid

Subscript and superscript

M	The number of the outer grid
N	The circumferential number of the last grid
m, n	The index of the grid

Greek symbols

τ	Time
ε	The emissivity coefficient for the tube surface
σ	The Stefan–Boltzmann constant
θ	The angle at the circumference of the grid
α	The angle between the ray and the radial direction
$\Delta r, \Delta\theta, \Delta\tau$	The radial length, angle of the grid and the unit time
λ	Thermal conductivity

References

[1] H.E. YaLing, W. Kun, D.U. BaoCun, Q.I.U. Yu, Z. ZhangJing, L. Qi, Non-uniform characteristics of solar flux distribution in the concentrating solar power systems and its corresponding solutions: a review, Chin. Sci. Bull. 61 (30) (2016), 3208.

[2] H.L. Zhang, J. Baeyens, J. Degrève, G. Cacères, Concentrated solar power plants: review and design methodology, Renew. Sustain. Energy Rev. 22 (2013) 466–481.

[3] Z. Yao, Z. Wang, Y.-H. Kang, J.-K. Kim, X. Wei, Theoretical simulation investigation of the pioneer 1 Mw solar power tower system in China, in: D.Y. Goswami, Y. Zhao (Eds.), Proceedings of ISES World Congress 2007, I – vol. V, Springer Berlin Heidelberg, Berlin, Heidelberg, 2009, pp. 1733–1737.

[4] W.-Q. Wang, Y. Qiu, M.-J. Li, Y.-L. He, Z.-D. Cheng, Coupled optical and thermal performance of a fin-like molten salt receiver for the next-generation solar power tower, Appl. Energy 272 (2020), 115079.

[5] C. Zou, Y. Zhang, Q. Falcoz, P. Neveu, C. Zhang, W. Shu, S. Huang, Design and optimization of a high-temperature cavity receiver for a solar energy cascade utilization system, Renew. Energy 103 (2017) 478–489.

[6] C. Zou, Y. Zhang, H. Feng, Q. Falcoz, P. Neveu, W. Gao, C. Zhang, Effects of geometric parameters on thermal performance for a cylindrical solar receiver using a 3D numerical model, Energy Convers. Manag. 149 (2017) 293–302.

[7] M.R. Rodríguez-Sánchez, C. Marugan-Cruz, A. Acosta-Iborra, D. Santana, Comparison of simplified heat transfer models and CFD simulations for molten salt external receiver, Appl. Therm. Eng. 73 (1) (2014) 993–1005.

[8] H. Zhou, Y. Li, M. Zhou, D. Liu, Y. Zhu, W. Fang, Numerical simulation of a lab-scale molten-salt external solar receiver and its experimental validation, J. Energy Eng. 147 (1) (2021), 04020074.

[9] H. Zhou, Y. Li, Y. Zhu, W. Fang, D. Liu, M. Zhou, K. Cen, Experimental and numerical evaluation of a lab-scale external solar receiver, J. Renew. Sustain. Energy 12 (4) (2020), 043705.

[10] H. Zhou, Y. Li, Y. Zuo, M. Zhou, W. Fang, Y. Zhu, Thermal performance and thermal stress analysis of a 600 MWth solar cylinder external receiver, Renew. Energy 164 (2021) 331–345.

[11] M. Fernández-Torrijos, C. Sobrino, C. Marugán-Cruz, D. Santana, Experimental and numerical study of the heat transfer process during the startup of molten salt tower receivers, Appl. Therm. Eng. 178 (2020).

[12] M. Fernández-Torrijos, C. Sobrino, J.A. Almendros-Ibáñez, C. Marugán-Cruz, D. Santana, Inverse heat problem of determining unknown surface heat flux in a molten salt loop, Int. J. Heat Mass Tran. 139 (2019) 503–516.

[13] Z. Wan, J. Fang, N. Tu, J. Wei, M.A. Qaisrani, Numerical study on thermal stress and cold startup induced thermal fatigue of a water/steam cavity receiver in concentrated solar power (CSP) plants, Sol. Energy 170 (2018) 430–441.

[14] G.W. Lopez, Startup modeling of the receiver of NASA's 2-kilowatt solar dynamic power system, J. Propul. Power 15 (3) (1999) 424–431.

[15] B.E. Hefni, Detailed Dynamic Model for the Gravity Drainage of a Tower Solar Receiver, with ThermoSysPro Library - Time Needed to Completely Drain the Receiver and Salt Temperature as a Function of the Ambient Conditions, SOLARPACES 2018, International Conference on Concentrating Solar Power and Chemical Energy Systems, 2019.

[16] L. Yang, R. Zhou, X. Jin, X. Ling, H. Peng, Experimental investigate on thermal properties of a novel high temperature flat heat pipe receiver in solar power tower plant, Appl. Therm. Eng. 109 (2016) 610–618.

[17] L. Yang, X. Ling, H. Peng, L. Duan, X. Chen, Starting characteristics of a novel high temperature flat heat pipe receiver in solar power tower plant based of"Flat-front"Startup model, Energy 183 (2019) 936–945.

[18] X. Wang, T. Ma, Y. Zhu, H. Chen, J. Zeng, Experimental investigation on startup and thermal performance of a high temperature special-shaped heat pipe coupling the flat plate heat pipe and cylindrical heat pipes, Exp. Therm. Fluid Sci. 77 (2016) 1–9.

[19] W. Wang, A. Malmquist, L. Aichmayer, B. Laumert, Transient performance of an impinging receiver: an indoor experimental study, Energy Convers. Manag. 158 (2018) 193–200.

[20] T. Xu, G. Zhang, C. Peniguel, Z. Liao, X. Li, J. Lu, Z. Wang, Numerical Study of Cold Filling and Tube Deformation in the Molten Salt Receiver, 2017.

[21] S.O. Alexopoulos, J. Dersch, M. Roeb, R. Pitz-Paal, Simulation model for the transient process behaviour of solar aluminium recycling in a rotary kiln, Appl. Therm. Eng. 78 (2015) 387–396.

[22] R.W. Bradshaw, D.B. Dawson, W. De La Rosa, R. Gilbert, S.H. Goods, M.J. Hale, P. Jacobs, S.A. Jones, G.J. Kolb, J.E. Pacheco, M.R. Prairie, H.E. Reilly, S.K. Showalter, L.L. Vant-Hull, Final Test and Evaluation Results from the Solar Two Project, 2002. United States.

[23] A. Bejan, A.D. Kraus, Heat Transfer Handbook, John Wiley & Sons, 2003.

[24] S. Yang, W. Tao, Heat transfer[M], Fourth Edition, Higher Education Press, Beijing, 2006.